공학석사 학위논문

# Calculation of ion species fraction of $BF_3$ discharge in non-Maxwellian plasma

## 비-멕스웰 분포함수를 가지는 $BF_3$ 방전의 이온 분율 계산

2021 년 08월

서울대학교 대학원

에너지시스템공학부

반두이

# Calculation of ion species fraction of $BF_3$ discharge in non-Maxwellian plasma

지도교수 정 경 재

이 논문을 공학석사 학위논문으로 제출함

2021 년 07 월

서울대학교 대학원

에너지시스템공학부

반두이

반두이의 공학석사 학위논문을 인준함

2021 년 07 월

위 원 장 황 용 석

부위원장 정 경 재

위 원 김 준 영

# Abstract

# Calculation of ion species fraction of $BF_3$ discharge in non-Maxwellian plasma

Cung Van Duy
Department of Energy System Engineering
(Nuclear Engineering)
College of Engineering
Seoul National University

The $0^{th}$-dimensional global model of $BF_3$ plasma discharge has been developed in the low-pressure regime to calculate ion species fractions. The simple model considers equations of the particle balance, the charge conservation, and the particle number conservation. Especially, to reflect the nature of non-Maxwellian electron energy distribution in low-pressure discharges, the electrons are divided into two groups and their proportion is adjusted to see the change of ion species fraction.

The main purpose of the thesis is considering the change in ion species fraction when including the high-energy electrons group while fixing the low-energy electrons group and the recombination coefficient is not mentioned. The important contribution in the thesis is using the non-Maxwellian electron energy distribution function to calculate the

rate constant. Calculations using only low energy electron groups showed remarkably high sensitivity of the ion beam fraction to electron temperature, and the sensitivity could be mitigated by adding the high energy electron ratio. Furthermore, the recombination coefficient and the high-energy electrons fraction values also played the major role in the model. These parameters can be changed to produce the desired ion species fractions in the model.

Keywords: Ion species fraction, $BF_3$ discharge, Particle balance equation, Charge conservation

Student number: 2018-27587

# Table of Contents

# List of Figures

# List of Tables

# List of Abbreviations

e : Elementary charge
$\varepsilon_0$ : Permittivity of free space
$T_e$ : Electron temperature
$T_{eff}$ : Effective electron temperature
σ : Cross-section
E : Electron energy
k : Rate constant
α : Fine structure constant
N : Orbital electron occupation number
T : Incident electron energy
U : Orbital kinetic energy
B : Orbital binding energy, Magnetic field
R : Rydberg energy, Radius, Plasma radius
$a_0$ : Bohr radius
$E_{iz}$ : Ionization energy
I : Ionization potential
A : Bethe coefficient, Surface area of the chamber wall
$\sigma_{ph}$ : Photoionization cross-section
$I_i$ : Total ion current
$I_e$ : Electron beam intensity
L : Length
p : Gas pressure (or Operating pressure)
$n_e$ : Electron density (or Plasma density)
$T_0$ : Ion temperature, Neutral temperature
$N_0$ : $BF_3$ molecules density before discharge
$T_i$ : Transit time of the $i^{th}$ neutral species, Ion temperature
$\gamma$ : Recombination coefficient
$\tau_i$ : Containment time of the $i^{th}$ ion species, Ion confinement time

$m_e$ : Electron mass

$k_B$ : Boltzmann constant

$g_p$ : Electron energy probability function (EEPF)

$T_l$ : Electron temperature of the low-energy electrons

$T_h$ : Electron temperature of the high-energy electrons

$n_{l,0}$ : Electron density of the low electron groups at the discharge center

$n_{h,0}$ : Electron density of the high electron groups at the discharge center

V : Source chamber volume

# Chapter 1. Introduction

## 1.1. Penning Ionization Gauge Source

### 1.1.1. General Description

L. R. Maxwell invented the Penning discharge in 1931 [1, 12]. The name of the Penning ion source was given by F. M. Penning who investigated the Penning ionization vacuum Gauge in 1937 [1, 12]. The Penning ion source scheme and circuitry are shown in Figure 1.1 [1]. It includes a hollow anode cylinder with one cathode on each end [1]. The electrons are confined inside the anode and kept fluctuating between the cathodes by a strong axial magnetic field, which leads to a large ionization efficiency [1]. The type of cathodes may be cold or hot (Figure 1.1a) or one filament and a cold anticathode (Figure 1.1b) or an indirectly heated block cathode and a cold anticathode (Figure 1.1c) [1, 19]. In general, the anticathode is connected to the cathode, except in some cyclotrons [1].

Figure 1.5 illustrates the method of ion extraction from the PIG source [1]. They are axial extraction (Figure 1.2a) through one cathode or radial extraction through a slit in the anode (Figure 1.2b) [1]. The radial ion extraction method is more popular in PIG sources [1]. Gas is fed to the discharge through the anode close to the cathodes to promote the ignition of the arc and maintain the neutral gas flow through the extraction slit in the anode low [1].

PIG source can be worked in DC or pulsed mode, depending on the working mode of the accelerator and the required power level for the production of a specific ion beam [1]. The range of values of arc

voltage for the PIG source may be between a few hundred V and several kV, and the arc current values can be from some mA to tens of A, depending on the cathode type and the gas pressure [1]. The magnetic field is from 0.1 to 1 T and is usually homogeneous [1].

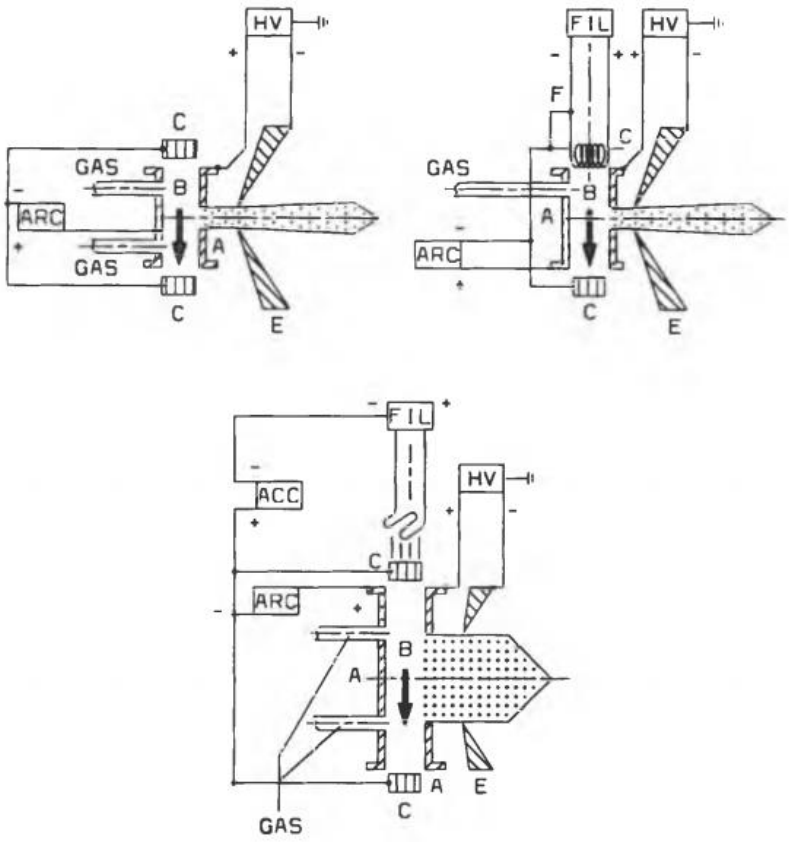


Figure 1.1. Penning ion source scheme and circuitry: (a) cold cathodes, (b) filament cathode, and (c) heated cathode [1].

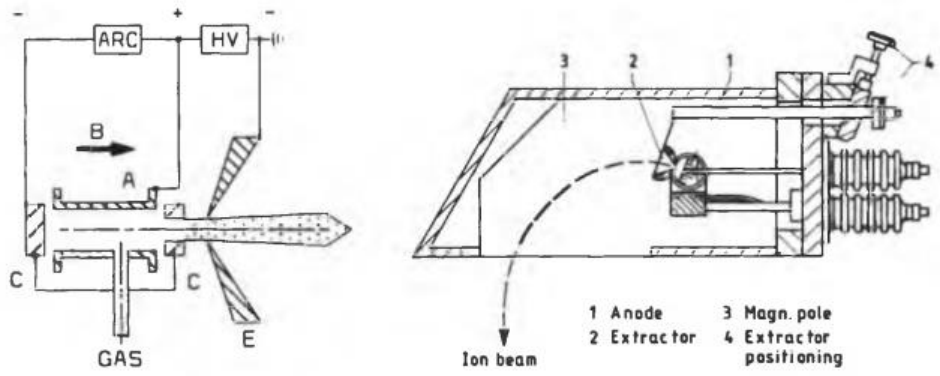


Figure 1.2. PIG ion source with axial (a) and radial (b) extraction [1].

### 1.1.2. Important factors in the model of the PIG source

In the thesis, the axial magnetic field effect is not mentioned in the model, so there are only two important factors in the model: the gas pressure of the Penning discharge and the electron energy distribution. The Penning discharge includes two main regions: a low-pressure region from 7.50 x $10^{-6}$ to 7.50 mTorr and a high-pressure region from 0.75 and 750.00 mTorr [1]. The high-pressure region is more important for ion sources, which contains two types: the cold cathode PIG source with arc voltages above 1 kV and currents from 0.5 to 5 A, and the hot cathode PIG source with arc voltages below 1 kV and currents from 1 to 50 A, which are given in Figure 1.3 [1]. In this model, the gas pressure is chosen from the low-pressure region.

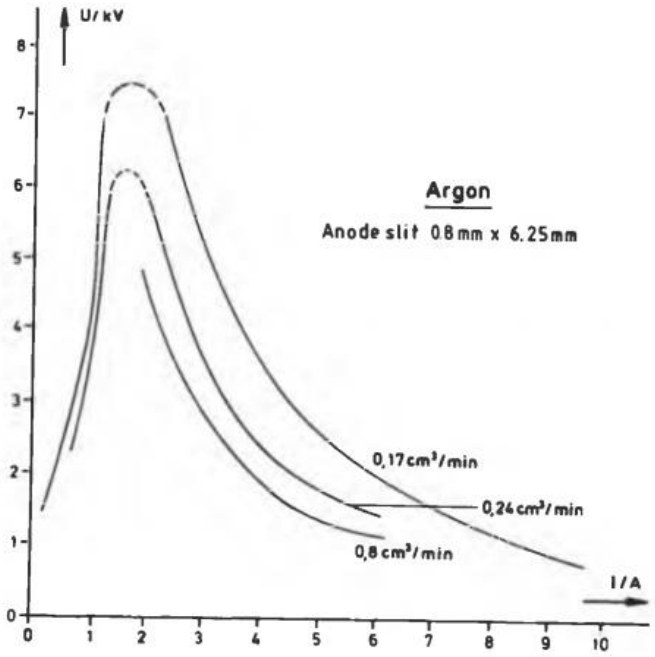


Figure 1.3. Discharge characteristics of a PIG source in a cold cathode and a hot cathode mode [1].

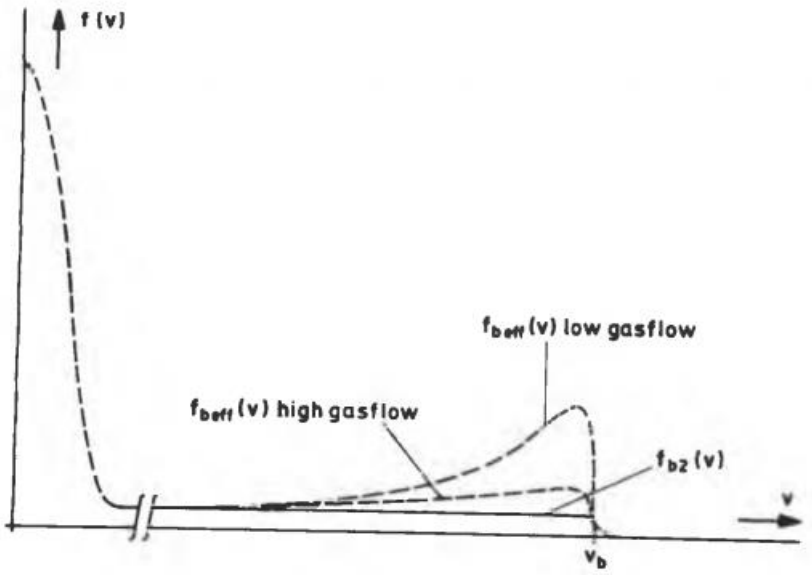


Figure 1.4. Electron energy distribution in a PIG ion source [1].

Figure 1.4 describes the electron energy distribution in a PIG ion source [1]. The energy distribution of electrons generated from the cathodes is depended on the cathode temperature or the secondary emission process [1]. These electrons are accelerated in the cathode sheath [1]. More than half of these electrons can come to the opposite cathode and are lost for the ionization process [1]. Other electrons can fluctuate many times between the cathodes or become thermalized in the dense plasma within a few oscillations [1]. A background of low-energy electrons, which is made by secondary electrons, can have enough energy by local fluctuating ranges to participate in the ionization process [1]. Eight ions or charges on average can be generated from one electron [1]. Electrons can reach the anode throughout the magnetic field lines, accelerated by local ranges of plasma fluctuations [1]. For the PIG source, the EEPF is non-Maxwellian, so these obtained experimental EEPF data are given by the sum of the Maxwellian electron energy distribution function with each low and high temperature to be simplified [10]. The formula of the EEPF from the Maxwellian electron energy distribution function will be mentioned in Chapter 2.

The arc current controls the discharge and the arc voltage or particle density in the discharge chamber goes up while the gas flow goes down until the discharge turns unstable (Figure 1.5) [1]. The values of ion current of cathodes are equal to each other for the cold cathode PIG ion sources, while in the heated cathode PIG sources, the larger proportion of ion current arrives the cathode with rising the amount of heating or emission of the cathode compared to the cold anticathode [1]. The value of ion current to the anode is equal to that to the cathode, so the ion current density at the cathodes is five to ten times the density at the anode surface, then the extracted current densities give the same relation [1].

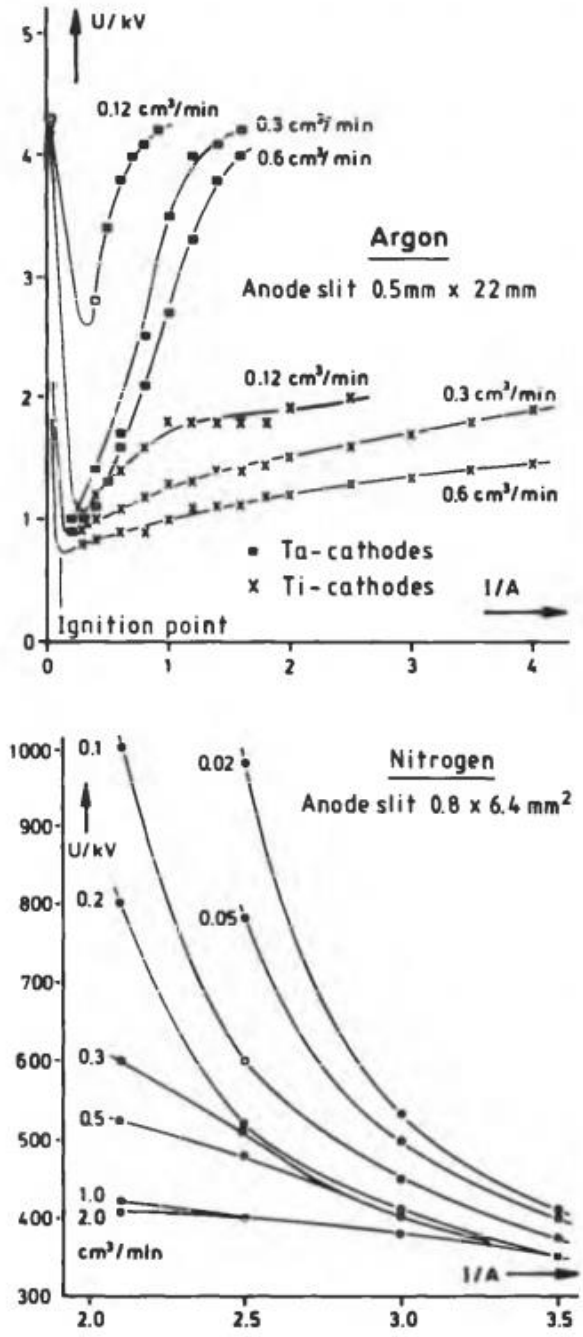


Figure 1.5. Variation of arc characteristics for different gas flows (a) cold cathodes and (b) hot cathodes [1].

### 1.1.3. Multiply Charged Ions

For the PIG sources, multiply charged ions may be generated powerful, because of the high plasma density ($n_e < 10^{13}$ $cm^{-3}$), the high primary electron energy, low gas pressure, or high degree of ionization, and a reasonable ion confinement time [1]. The ion confinement time can be given by $\tau_i = R^2B/T_e$, where R is the plasma radius (cm), B is the magnetic field (T), and $T_e$ is the electron temperature (eV) [1]. For the common PIG source parameters in generating multiply charged ion, $\tau_i \sim 10 - 100$ μs [1].

The yield of multiply charged ions rises with ion current or plasma density and with dropping gas pressure or neutral particle density [1]. The missing particles are adjusted by rising the arc voltage and generating multiply charged ions, which leads to bringing the desired current by the external circuit [1]. The arc turned into unstable and is eliminated when this compensation is impossible [1].

### 1.1.4. Metal Ion Production

In PIG sources, gaseous compounds, chemical synthesis, evaporation, and sputtering are used to produce metallic ions or ions from nongaseous materials [1]. In most cases, sputtering is used when the melting temperature of the substance is not too low [1]. The melting temperature of an electrode can be risen by using alloys [1]. Overall, the position of the sputtering electrode is in a slit in the anode wall opposite or next to the extraction slit (Figure 1.6a) and connected to about several hundred V potential, negative for the anode [1]. Half- or full-cylindrical sputter electrode shapes can also be used (Figure 1.6b) [1].

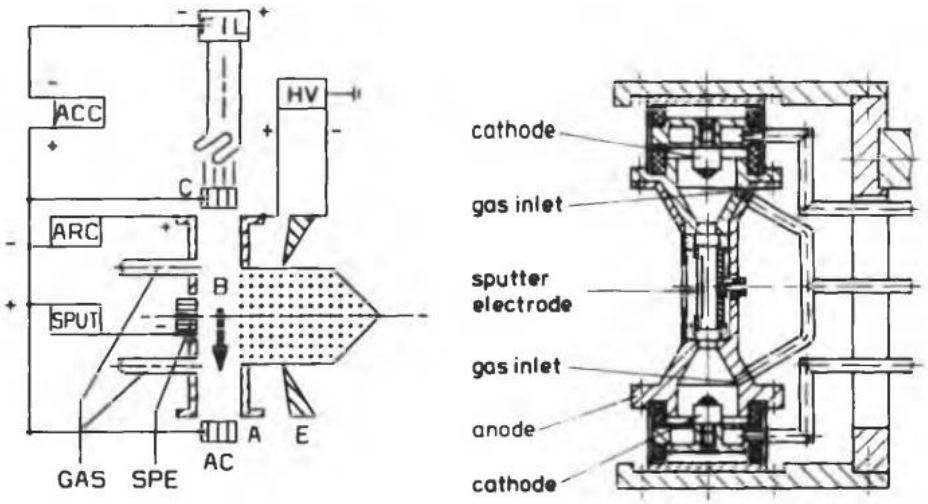


Figure 1.6. PIG sputter electrode arrangements: (a) block shape and (b) cylindrical shape [1].

## 1.2. Motivation

In this thesis, the global model is essential to estimate the optimal plasma parameters and the ion species fractions. In $BF_3$ discharge of the model, there are 5 neutral species (B, F, BF, $BF_2$, $BF_3$) and 5 ion species ($B^+$, $F^+$, $BF^+$, $BF_2^+$, $BF_3^+$). For instance, the ion species fraction of $B^+$ is given by:

$$Ion\ species\ fraction\ of\ B^+ = \frac{n_{B^+}}{n_{B^+}+n_{F^+}+n_{BF^+}+n_{BF_2^+}+n_{BF_3^+}}. \quad (1)$$

In (1), $n_{B^+}$, $n_{F^+}$, $n_{BF^+}$, $n_{BF_2^+}$, $n_{BF_3^+}$ are the densities of $B^+$, $F^+$, $BF^+$, $BF_2^+$, $BF_3^+$, respectively. According to Fukumasa et al [11], Choe [12], Zorat et al [13], Martin and Green [19], the charge conservation is determined from the quasineutrality condition:

$$n_{B^+} + n_{F^+} + n_{BF^+} + n_{BF_2^+} + n_{BF_3^+} = n_e. \quad (2)$$

From (1) and (2), the ion species fraction of $B^+$ is $n_{B^+}/n_e$. The formulas of ion species fractions for the remaining ion species are also the same as in the case of $B^+$.

In the previous modeling work, Patel et al [2, 3] assumed the Maxwellian EEPF with the multi-cusp magnetic field structure for the ULE2 ion source. However, the magnetic field effect which is used in the PIG source is the axial magnetic field effect as mentioned above, and it is completely different compared to the Patel et al [2, 3]. Figure 1.7 shows the schematic representation of the ULE2 ion source [2, 3]. Only the Maxwellian electron energy distribution function was considered in Patel's work as mentioned above [2, 3]. That is the limitation of Patel's work.

In a DC plasma source with a magnetic field and low-pressure operation, especially the PIG source in this thesis, the radial profile of plasma properties is non-uniform. In addition, the obtained

experimental EEPF data are observed to be non-Maxwellian. Therefore, the motivation in this study is using the non-Maxwellian EEPF data in the global model to calculate the ion species fractions. The important contribution in this thesis is using the experimental electron energy probability function (EEPF) to calculate the rate constant data, which are made to determine the ion species fraction after that.

The global model in this thesis is done from the $BF_3$ discharge in the PIG source. The PIG source has the cylindrical chamber with the axial magnetic field structure. Figures 1.8 and 1.9 describe the cross-section and the example of non-Maxwellian EEPF for the PIG source [9].

The purposes of the thesis are: (1) calculating the ion species fraction when using the Maxwellian electron energy distribution function, and (2) considering the change of ion species fraction when including the high-energy electrons group while fixing the low-energy electrons group and the recombination coefficient is not mentioned, in this case, the non-Maxwellian electron energy distribution function is used. The second purpose is the main goal of the thesis.

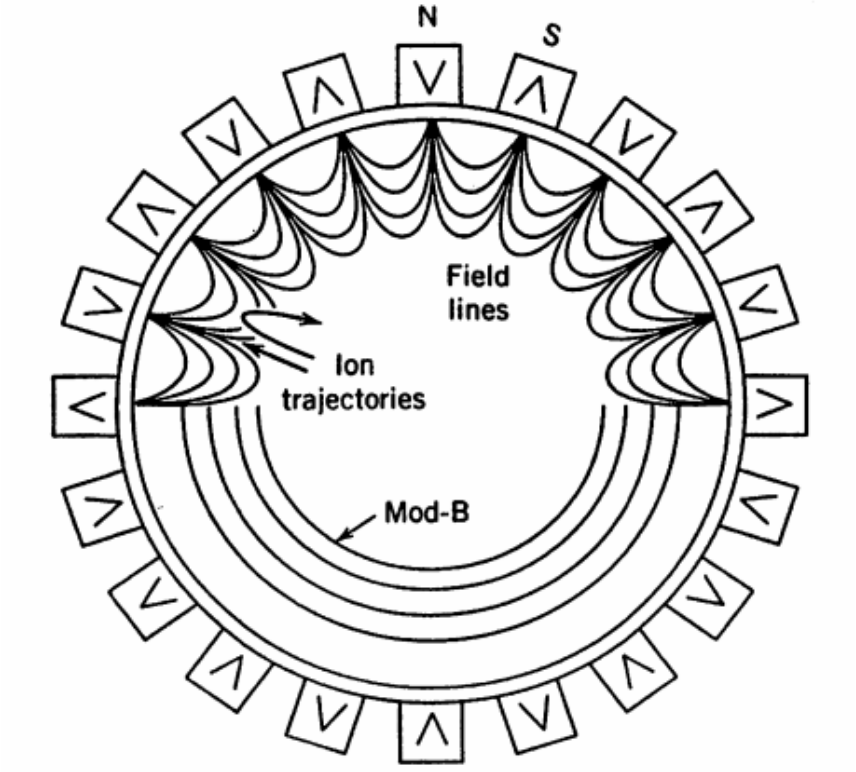


Figure 1.7. The ULE2 ion source cross-section [2, 3].

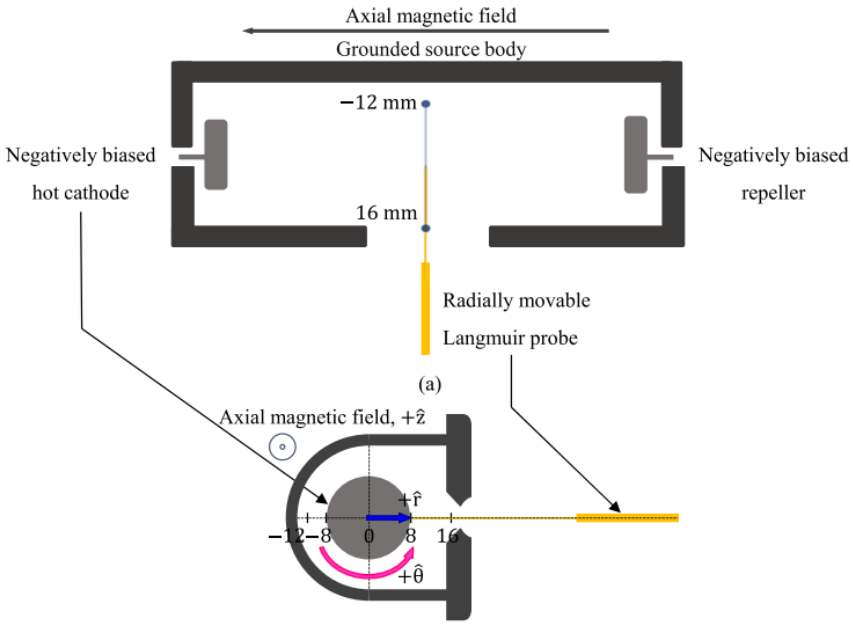


Figure 1.8. The cross-section of the PIG source [9].

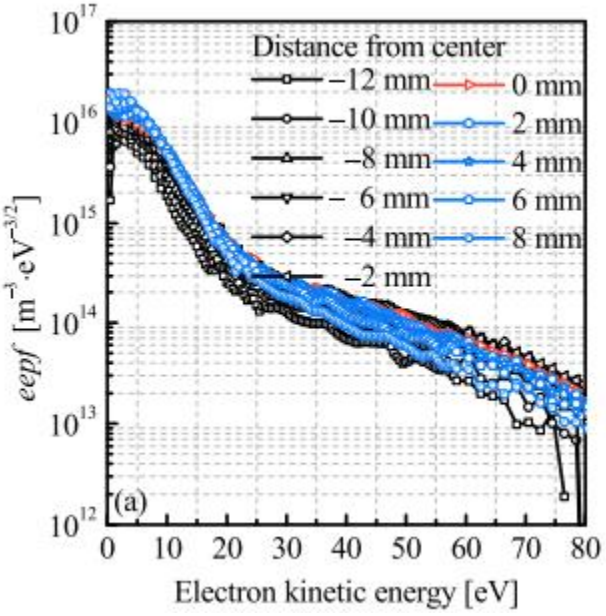


Figure 1.9. The example of the non-Maxwellian EEPF for the PIG source [9].

# Chapter 2. Global model

## 2.1. Assumptions

In this thesis, the cylindrical chamber of the PIG source with the radius R = 1.5 cm and the length L = 9 cm will be considered in the global model [8, 17]. The suppositions of the global model are [2, 3, 16]:

1. Considering the steady-state plasma [2, 3, 16].
2. The magnetic field is not included [16].
3. Considering the rate constants data which are calculated by using the obtained experimental EEPF data and isotropic particle velocity distributions [2, 3, 10, 16].
4. Supposing the constant neutral and ion temperatures based on Patel's work (600 K) [2, 3, 16].
5. Supposing all of the averaged volume densities [2, 3, 16]:
$$n = \frac{1}{\pi R^2 L}\left(2\pi \int_0^R R dr \int_0^L n(r,z) dz\right). \quad (3)$$
6. Considering the uniform density figures, except in the plasma sheath, the thickness of the sheath is small compared to the chamber size [2, 3, 16].
7. Threshold processes (dissociation, ionization) are caused by electrons entirely [2, 3, 16].
8. The kinds of electron–neutral reactions included are direct ionization, dissociative ionization, dissociation [2, 3, 16].
9. Ignoring three-body interactions, two-step ionization, negative ions, and metastables [2, 3, 16].
10. The wall recombination coefficients of all neutral species are identical [11, 12, 16].

11. The wall is a source of producing $BF_3$ entirely, and a sink for all other neutral species [2, 3, 16].
12. For the low-pressure region of plasma (< 50 mTorr) which is mentioned here, diffusion to the wall is the most important loss process for neutral species due to the low reaction rates of gas-phase recombination [2, 16].

From the assumptions which are expressed above and as mentioned in Chapter 1, the present model includes 5 neutral species (B, F, BF, $BF_2$, $BF_3$) and 5 ion species ($B^+$, $F^+$, $BF^+$, $BF_2{}^+$, $BF_3{}^+$). All of the reactions of the global model are given in Table 1.

Table 1. List of reactions [2, 3].

| Reactions | Energy [eV] | Rate constants [$m^3/s$] | Ref. |
|---|---|---|---|
| 1. $e + BF_3 \rightarrow BF_3^+ + 2e$ | 15.56 | $k_{01}$ | [2, 3, 5, 6, 16] |
| 2. $e + BF_3 \rightarrow BF_2^+ + F + 2e$ | 15.76 | $k_{02}$ | [2, 3, 4, 16] |
| 3. $e + BF_3 \rightarrow BF_2 + F + e$ | 10.10 | $k_{03}$ | [2, 3, 4, 16] |
| 4. $e + BF_2 \rightarrow BF_2^+ + 2e$ | 9.40 | $k_{04}$ | [2, 3, 5, 6, 16] |
| 5. $e + BF_2 \rightarrow BF + F + e$ | 5.90 | $k_{05}$ | [2, 3, 4, 16] |
| 6. $e + BF \rightarrow BF^+ + 2e$ | 11.12 | $k_{06}$ | [2, 3, 5, 6, 16] |
| 7. $e + BF \rightarrow B + F + e$ | 8.10 | $k_{07}$ | [2, 3, 4, 16] |
| 8. $e + B \rightarrow B^+ + 2e$ | 8.30 | $k_{08}$ | [2, 3, 5, 6, 16] |
| 9. $e + F \rightarrow F^+ + 2e$ | 17.40 | $k_{10}$ | [2, 3, 7, 16, 20] |

## 2.2. Description of the model for PIG source

To implement the calculation, the $0^{th}$ – dimensional global model is used with three types of equations [11, 12, 13, 15, 16, 19]. They are particle balance equation, charge conservation equation, and particle conservation equation. The power balance equation and the axial magnetic field effect of the ion source are not mentioned because of the growth of the complication of the model, which requires to take more time to obtain accurate results. The basic assumptions of the model are mentioned in section 2.1. The ion species ratios are calculated in a steady-state plasma [2, 11, 12, 15, 16, 19]. The particle balance equations for all neutral and ion species are given below [11, 12, 15, 16, 19]:

$$N_3 n_e k_{07} - N_1 n_e k_{08} - \gamma N_1/T_1 = 0 \quad (4)$$

$$N_5 n_e k_{02} + N_5 n_e k_{03} + N_4 n_e k_{05} + N_3 n_e k_{07} - N_2 n_e k_{09} - \gamma N_2/T_2 = 0 \quad (5)$$

$$N_4 n_e k_{05} - N_3 n_e k_{06} - N_3 n_e k_{07} - \gamma N_3/T_3 = 0 \quad (6)$$

$$N_5 n_e k_{03} - N_4 n_e k_{04} - N_4 n_e k_{05} - \gamma N_4/T_4 = 0 \quad (7)$$

$$N_1 n_e k_{08} - n_1/\tau_1 = 0 \quad (8)$$

$$N_1 n_e k_{09} - n_2/\tau_2 = 0 \quad (9)$$

$$N_3 n_e k_{06} - n_3/\tau_3 = 0 \quad (10)$$

$$N_5 n_e k_{02} + N_4 n_e k_{04} - n_4/\tau_4 = 0 \quad (11)$$

$$N_5 n_e k_{01} - n_5/\tau_5 = 0\,. \quad (12)$$

The charge and particle number conservations are [11, 12, 15, 16, 19]:

$$n_1 + n_2 + n_3 + n_4 + n_5 = n_e \quad (13)$$

$$N_1 + \frac{1}{3}N_2 + N_3 + N_4 + N_5 = N_0 = p/kT_0, \quad (14)$$

where $N_1$, $N_2$, $N_3$, $N_4$, $N_5$ are the densities of B, F, BF, $BF_2$, $BF_3$,

respectively; $n_1$, $n_2$, $n_3$, $n_4$, $n_5$ are the densities of $B^+$, $F^+$, $BF^+$, $BF_2^+$, $BF_3^+$, respectively; $T_1$, $T_2$, $T_3$, $T_4$ are the transit times of B, F, BF, $BF_2$ across the chamber, respectively; the containment times of $B^+$, $F^+$, $BF^+$, $BF_2^+$, $BF_3^+$ are $\tau_1$, $\tau_2$, $\tau_3$, $\tau_4$, $\tau_5$, respectively; and the containment times of B, F, BF, $BF_2$ would be $T_1/\gamma$, $T_2/\gamma$, $T_3/\gamma$, $T_4/\gamma$; $\gamma$ is the recombination coefficient of B, F, BF, $BF_2$ at the wall; p is the $BF_3$ gas pressure; $T_0$ is the ion and neutral temperature (600 K); $n_e$ is the electron density; $N_0$ is the density of $BF_3$ molecules before discharge [2, 11, 12, 15, 16, 19]. The coefficients from $k_{01}$ to $k_{08}$ are the rate constants corresponding to the reactions from 1 to 8, respectively.

In the equations which are expressed above, the ratio of $\tau_1$, $\tau_2$, $\tau_3$, $\tau_4$, $\tau_5$ is considered to be the ratio of the square root of the respective ion masses, the ratio of $T_1$, $T_2$, $T_3$, $T_4$ is also considered to be the ratio of the square root of the respective atomic or molecular masses [11, 12, 15, 16, 19]. $\tau_1$ is calculated as one unknown variable, while $T_1 = 4V/v_0 A$ where V is the source chamber volume, A is the surface area of the chamber wall and $v_0$ is the mean velocity of B atoms [11, 15, 19]. The particle number conservation equation is set up by assuming that the total density of the neutral particles is a constant [15]. The charge conservation equation is built based on the assumption that ionization is produced by thermal electrons [15, 19]. The axial magnetic field effect of the ion source [8, 17] is not mentioned in this model.

The main parameters to determine the ion species fraction are the electron density, the effective electron temperature, and the recombination coefficient. The plasma density and the effective electron temperature are known parameters, while the recombination coefficient is the free parameter. The physical meaning of the recombination coefficient $\gamma$ is: atoms (or molecules) only partially recombine at the wall, so the loss rate of the $i^{th}$ neutral species is $\gamma N_i/T_i$, where $N_i$ and $T_i$ are the density and the transit time of the $i^{th}$ neutral

species, respectively [11, 12, 15, 19]. When the recombination coefficient is equal to zero, all neutral species come back to the plasma as the same species if they come to the wall. If the recombination coefficient value is unity, all neutral species recombine to $BF_3$ and come back to the wall as $BF_3$. The pressure is determined based on its dependence on the gas flow rate in the experimental data. The gas pressure goes up when rising the gas flow rate. The plasma density and the electron temperature are calculated based on the experimental conditions. The detailed information on these parameters will be mentioned in Chapter 2. Because there are no experimental results of the recombination coefficient, the value of this parameter is assumed to be from $10^{-6}$ to 1 [12].

## 2.3. Methods of calculation

The methods of solving equation systems in section 1.3 are referred from Choe [12] with Patel [2], Fukumasa et al [11], Martin and Green [19] and given in the MATLAB codes. From the equations system which is expressed in section 2.2, the variables below have been setup because the ion species fractions need to be calculated.

For neutrals species:

$$x(i) = \frac{N_i}{n_e} \tag{15}$$

where $n_e$ is the plasma density, $N_i$ is the density of the $i^{th}$ neutral species, i = 1 – 5 corresponding to B, F, BF, $BF_2$, $BF_3$, respectively in section 2.2.

For ions species:

$$x(i+5) = \frac{n_i}{n_e} \tag{16}$$

where $n_e$ is the plasma density, $n_i$ is the density of the $i^{th}$ neutral species, i = 1 – 5 corresponding to $B^+$, $F^+$, $BF^+$, $BF_2^+$, $BF_3^+$, respectively in section 2.2. This formula is also the ion species fraction as mentioned in section 1.2.

The ratio of $\tau_1$, $\tau_2$, $\tau_3$, $\tau_4$, $\tau_5$ is considered to be the ratio of the square root of the respective ion masses, hence:

$$\tau_1 : \tau_2 : \tau_3 : \tau_4 : \tau_5 = \sqrt{11} : \sqrt{19} : \sqrt{30} : \sqrt{49} : \sqrt{68}. \tag{17}$$

The ratio of $T_1$, $T_2$, $T_3$, $T_4$ is also considered to be the ratio of the square root of the respective atom or molecular masses, hence:

$$T_1 : T_2 : T_3 : T_4 = \sqrt{11} : \sqrt{19} : \sqrt{30} : \sqrt{49}. \tag{18}$$

The variable below has also been setup:

$$x(11) = \frac{1}{\tau_1}. \tag{19}$$

All of the 11 equations above in section 2.2 can be modified to the equations system below:

$$x(3)k_{07} - x(1)k_{08} - \frac{\gamma}{n_e T_1}x(1) = 0 \tag{20}$$

$$x(5)k_{02} + x(5)k_{03} + x(4)k_{05} + x(3)k_{07} - x(2)k_{09} - \frac{\gamma}{n_e T_1}x(2)\sqrt{\frac{11}{19}} = 0 \tag{21}$$

$$x(4)k_{05} - x(3)k_{06} - x(3)k_{07} - \frac{\gamma}{n_e T_1}x(3)\sqrt{\frac{11}{30}} = 0 \tag{22}$$

$$x(5)k_{03} - x(4)k_{04} - x(4)k_{05} - \frac{\gamma}{n_e T_1}x(4)\sqrt{\frac{11}{49}} = 0 \tag{23}$$

$$x(1)k_{08} - \frac{1}{n_e}x(6)x(11) = 0 \tag{24}$$

$$x(2)k_{09} - \frac{1}{n_e}x(7)x(11)\sqrt{\frac{11}{19}} = 0 \tag{25}$$

$$x(3)k_{06} - \frac{1}{n_e}x(8)x(11)\sqrt{\frac{11}{30}} = 0 \tag{26}$$

$$x(5)k_{02} + x(4)k_{04} - \frac{1}{n_e}x(9)x(11)\sqrt{\frac{11}{49}} = 0 \tag{27}$$

$$x(5)k_{01} - \frac{1}{n_e}x(10)x(11)\sqrt{\frac{11}{68}} = 0 \tag{28}$$

$$x(6) + x(7) + x(8) + x(9) + x(10) - 1 = 0 \tag{29}$$

$$x(1) + \frac{1}{3}x(2) + x(3) + x(4) + x(5) - \frac{N_0}{n_e} = 0. \tag{30}$$

In these equations, from the 1st equation to the 9th equation, the left-hand side and the right-hand side are divided to $n_e{}^2$, while in the last two equations, the left-hand side and the right-hand side are divided to $n_e$. After modifying 11 equations, the equation system is obtained, including 9 nonlinear equations and 2 linear equations, so this is the nonlinear equations system.

## 2.4. Present cross-section data

### 2.4.1. BEB cross-section

The present cross-section data is only considered for the primary reactions. The formula of BEB cross-section is used for the ionization reactions of $BF_3$, $BF_2$, BF, and B (reactions 1, 4, 6, and 8, respectively), where:

Nonrelativistic BEB cross-section [5, 6]:

$$\sigma_{BEB} = \frac{S}{t+u+1}\left[\frac{\ln t}{2}\left(1-\frac{1}{t^2}\right)+1-\frac{1}{t}-\frac{\ln t}{t+1}\right]. \quad (31)$$

In these formulas, $S = 4\pi\, a_0{}^2\, N\,(R/B)^2$, $t = T/B$, $u = U/B$, N is the orbital electron occupation number, T is the incident electron energy (eV), U is the orbital kinetic energy (eV), B is the orbital binding energy (eV), R is the Rydberg energy (= 13.6 eV), and $a_0$ is the Bohr radius (= 0.529 Å) [5, 6].

### 2.4.2. Thomson cross-section

The Thomson cross-section [2, 4] is used for the dissociative ionization of $BF_3$ (reaction 2), where:

$$\sigma_{iz}(E) = \begin{cases} 0, & E < E_{iz} \\ \pi\left(\frac{e}{4\pi\varepsilon_0}\right)^2 \frac{1}{E}\left(\frac{1}{E_{iz}}-\frac{1}{E}\right), & E > E_{iz} \end{cases}, \quad (32)$$

where $E_{iz}$ is the ionization energy (eV) [4].

### 2.4.3. Dissociation cross-section

The dissociation cross-section [2, 4] is used for the dissociation of $BF_3$, $BF_2$, BF (reactions 3, 5, and 7, respectively), where:

$$\sigma_{diss}(E) = \begin{cases} 0, & E < E_1 \\ \sigma_0 \frac{E - E_1}{E_1}, & E_1 < E < E_2 \\ \sigma_0 \frac{E_2 - E_1}{E}, & E > E_2 \end{cases}, \quad (33)$$

where:

$$\sigma_0 = \pi \left(\frac{e}{4\pi \sigma_0 E_1}\right)^2. \quad (34)$$

In this formula, $E_1$, $E_2$ are the dissociation and the ionization energy of the molecule (eV), respectively [2, 4].

### 2.4.4. Approximate Analytic Formula (AAF) cross-section

The Approximate Analytic Formula (AAF) by Lennon et al (1988) [7] and Bell et al (1983) [20] is used for the ionization of F (reaction 9), where:

$$\sigma(E) = \begin{cases} 0, & E < I \\ \frac{1}{IE}\left\{A \ln\frac{E}{I} + \sum_{i=1}^{N} B_i \left(1 - \frac{I}{E}\right)^i\right\}, & E \geq I \end{cases}. \quad (35)$$

In this formula, E is the incident electron energy (eV), I is the ionization potential (eV), A is the Bethe coefficient which is given by:

$$A = \frac{I}{\pi\alpha} \int_I^{\infty} \frac{\sigma_{ph}}{\epsilon} d\epsilon. \quad (36)$$

where $\sigma_{ph}$ is the photoionization cross-section, α is the fine structure constant [7, 20]. The cross-section data of the reactions are shown by the log-10 scales in Figure 2.1. Overall, from Figure 2.1, all of the cross-sections fluctuate when changing the electron energy.

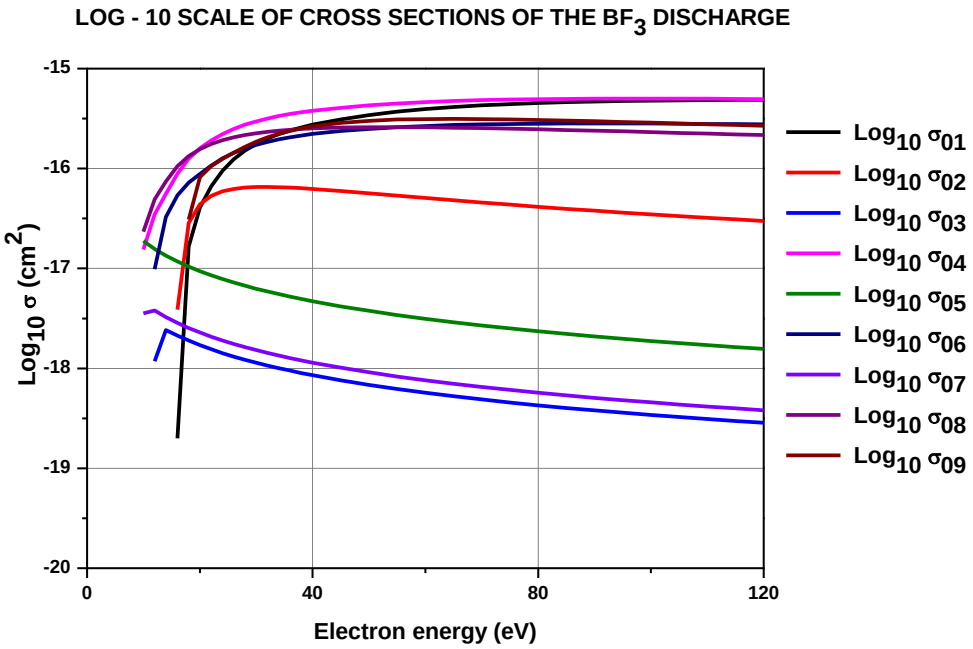


Figure 2.1. Cross-section data of the reactions for the $BF_3$ discharge.

## 2.5. Rate constant data

If the Maxwellian energy distribution function is assumed, the rate coefficients are calculated by [2]:

$$k_i = \langle \sigma v \rangle = 4\pi \int_0^{\infty} \sigma_i(v)\, v^3\, f(v)\, dv. \qquad (37)$$

where:

$$f(v) = \left(\frac{m_e}{2\pi\, k_B\, T_e}\right)^{3/2} \exp\left(-\frac{m_e\, v^2}{2 k_B\, T_e}\right) \qquad (38)$$

is the Maxwellian speed distribution function, $T_e$ is the electron temperature, σ is the collision cross-section, and $m_e$ is the electron mass [2]. In the present model, the Maxwellian energy distribution function will be considered, let $E = \frac{m_e\, v^2}{2}$ is the electron energy, transfer the unit of E and $k_B\, T_e$ [J] to E and $T_e$ [eV], then replacing to the integration above, the rate coefficient is given by [16]:

$$k_i = \left(\frac{2}{m_e}\right)^{1/2} \int_0^{\infty} \sigma_i(E)\, \sqrt{E}\, f_M(E)\, dE. \qquad (39)$$

where $f_M$ is the Maxwellian electron energy distribution function [16]:

$$f_M(E) = 2\sqrt{\frac{E}{\pi}}\, T_e^{-3/2} \exp\left(-\frac{E}{T_e}\right). \qquad (40)$$

When the electron energy probability function (EEPF) data is used in the thesis, the rate coefficients are determined by, for example in the case of the ionization process [4]:

$$k_{iz}(T_{eff}) = \frac{1}{n_e} \sqrt{\frac{2}{m_e}} \int_{E_{iz}}^{\infty} E\, \sigma_{iz}(E)\, g_p(E)\, dE. \qquad (41)$$

The rate coefficients of the other processes are also calculated by using the same formula as above. In this case, the obtained experimental EEPF data is given by the sum of the Maxwellian electron energy distribution function with each low and high temperature [10]:

$$g_p(E) = \frac{2}{\sqrt{\pi}} \frac{n_{l,0}}{T_l^{3/2}} \exp\left(-\frac{E}{T_l}\right) + \frac{2}{\sqrt{\pi}} \frac{n_{h,0}}{T_h^{3/2}} \exp\left(-\frac{E}{T_h}\right). \quad (42)$$

where $T_l$ and $T_h$ are the electron temperatures of the low and high-energy electrons, $n_{l,0}$ and $n_{h,0}$ are the electron density of the low and high electron groups at the discharge center, respectively [10]. The condition below must be satisfied for each position:

$$\alpha T_l + \beta T_h = T_{eff} \quad (43)$$

and:

$$\alpha + \beta = 1. \quad (44)$$

In (43) and (44), $\alpha = n_{l,0}/n_e$ and $\beta = n_{h,0}/n_e$. Besides the calculation results of the present rate constants, Patel's rate constant data is also used to make the comparisons later [2, 3]. The Patel's rate constant data is given by the Arrhenius form below [2, 3]:

$$k_i = a \,.\, T_e^b \,.\, e^{-\frac{c}{T_e}}. \quad (45)$$

The factors a, b, and c are given in Table 2. Figure 2.2 describes our calculation results of the rate constants of the reactions in the case of assuming the Maxwellian energy distribution function above by using the cross-section data in Figure 2.1. Figure 2.3 shows Patel's rate constant data in Table 2. Figure 2.4 describes the comparisons between our rate constant data in Figure 2.2 and Patel's data in Figure 2.3. From these figures and section 2.4, most of the present rate constants data are obtained by using the different cross-section data compared to Patel's calculation results [2, 3], such as the dissociative ionization of $BF_3$ (by using the Thomson cross-section), the dissociation of $BF_3$ (by using the Dissociation cross-section), the ionization of $BF_3$, $BF_2$, BF, B (by using the BEB cross-section of the NIST data [5, 6] because of this highly accurate level) and F (by using the Approximate Analytic Formula (AAF) [7, 20]), but they are not fit to the Arrhenius form [2] when performing the calculations. In addition, in the present rate

constants data, the value of electron temperature is from 1 to 100 eV, while in Patel's work, this value is from 1 to 8 eV. The reason for this difference is using the cross-sections data allows us to calculate the rate constants with the electron temperature larger than 8 eV. That is the limitation of Patel's work.

Table 2. The factors a, b, and c for the data of Patel's rate constants in the primary reactions [2, 3].

| Number | Primary Reaction | a ($10^{15}$) | b | c |
|---|---|---|---|---|
| 1 | $e + BF_3 \rightarrow BF_3^+ + 2e$ | 1.03 | 0.44 | 15.37 |
| 2 | $e + BF_3 \rightarrow BF_2^+ + F + 2e$ | 6.70 | 1.06 | 15.96 |
| 3 | $e + BF_3 \rightarrow BF_2 + F + e$ | 26.80 | 0.35 | 10.46 |
| 4 | $e + BF_2 \rightarrow BF_2^+ + 2e$ | 2.23 | 1.37 | 8.37 |
| 5 | $e + BF_2 \rightarrow BF + F + e$ | 133.00 | -0.41 | 6.77 |
| 6 | $e + BF \rightarrow BF^+ + 2e$ | 9.58 | 0.82 | 9.62 |
| 7 | $e + BF \rightarrow B + F + e$ | 37.30 | -0.42 | 8.97 |
| 8 | $e + B \rightarrow B^+ + 2e$ | 2.63 | 1.41 | 6.94 |
| 9 | $e + F \rightarrow F^+ + 2e$ | 13.00 | 0.00 | 16.50 |

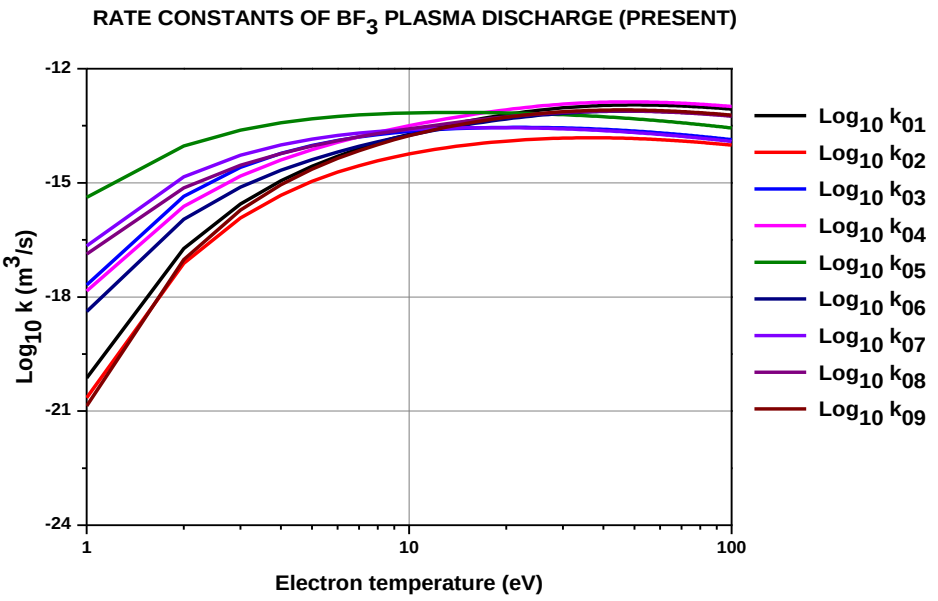


Figure 2.2. The present rate constants in the model.

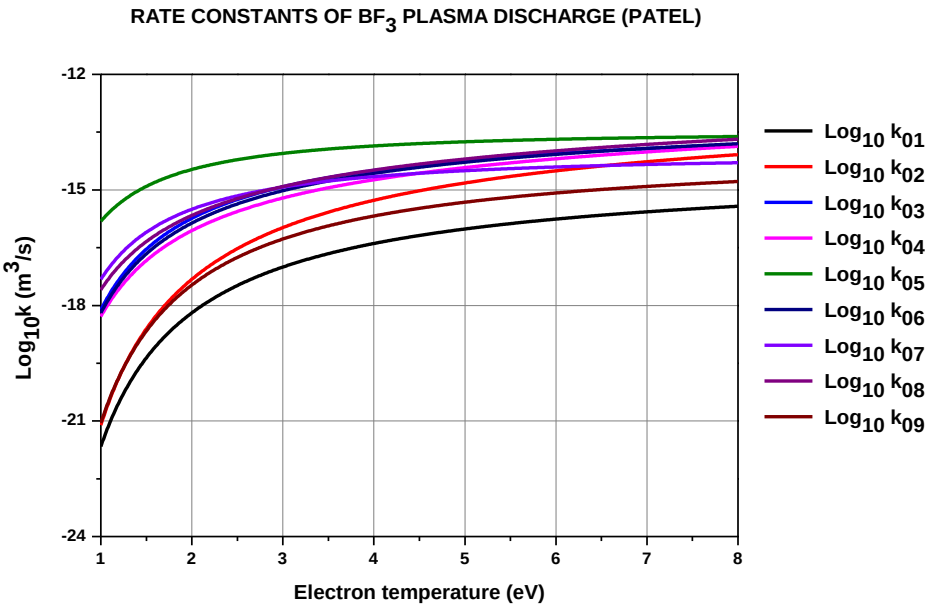


Figure 2.3. The Patel's rate constant data in the model [2, 3].

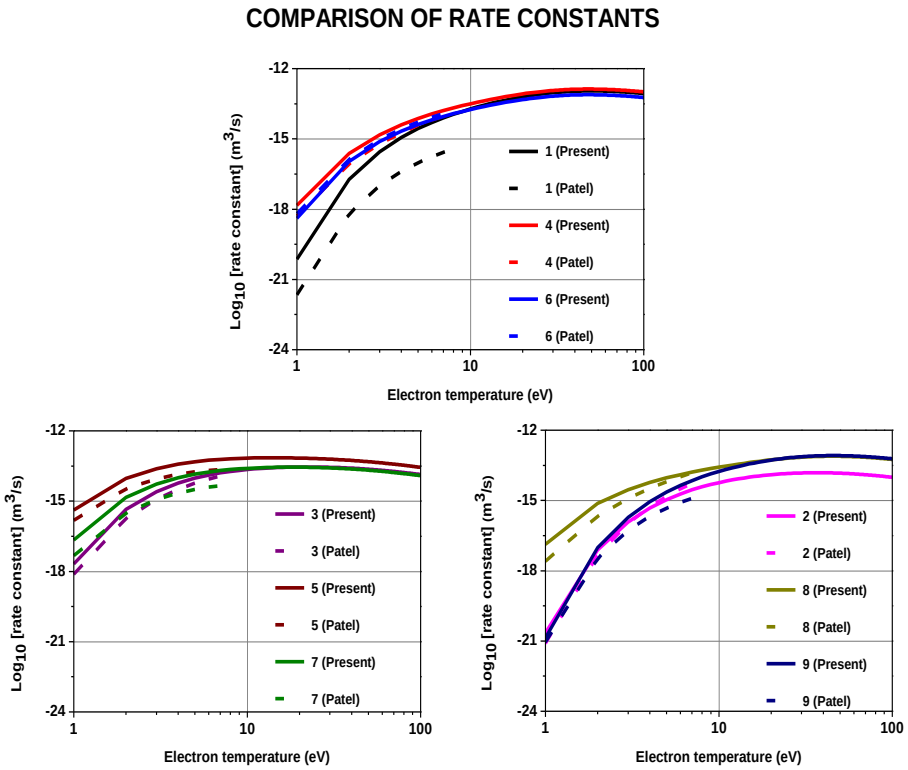


Figure 2.4. The comparisons between the present rate constant data (in Figure 2.2, solid line) and Patel's rate constant data (in Figure 2.3, dashed line) in the model.

## 2.6. Choosing parameters

In this thesis, the choice of values for plasma densities, effective electron temperatures, and operating pressures is taken based on the experimental conditions of $BF_3$ discharge in the PIG source [17]. The effective electron temperature and the plasma density have been obtained based on the experimental condition [17]. The plasma density and the effective electron temperature are determined based on the obtained experimental EEPF data [14, 17, 18]:

$$n_e = \int_0^\infty E^{1/2} g_p(E)\, dE \qquad (46)$$

$$eT_{eff} = \frac{2}{3n_e} \int_0^\infty E^{3/2} g_p(E)\, dE. \qquad (47)$$

# Chapter 3. Calculation results of the model by using the Maxwellian electron energy distribution function

## 3.1. Ion species fractions when changing recombination coefficient

In the model, the parameters such as recombination coefficient, plasma density, and effective electron temperature will be used to calculate. In addition, only the rate constant data which are calculated from the experimental data will be used to calculate.

Figure 3.1 shows the variation of ion species fraction when changing the recombination coefficient [12]. The gas pressure p is set as 3 mTorr, the plasma density $n_e$ $10^{18}$ $m^{-3}$, and the effective electron temperature $T_{eff}$ 3 eV [12]. From Figure 3.1, the ion species fractions of $BF_2^+$ and $BF_3^+$ increase when increasing the recombination coefficient, but the ion species fraction of $F^+$ decreases. The ion species fractions of $B^+$ and $BF^+$ fluctuate. The ion species fraction of $F^+$ is highest in most recombination coefficient values. The ion species fraction of $B^+$ is highest when the recombination coefficient $\gamma$ is approximately from 0.05 to 0.08. When the recombination coefficient $\gamma$ is approximately between 0.08 and 1, the ion species fraction of $BF_3^+$ is highest. The recombination coefficient need to be fallen to rise the ion species fraction of $F^+$, but this coefficient need going up to rise the ion species fraction of $BF_2^+$ or $BF_3^+$.

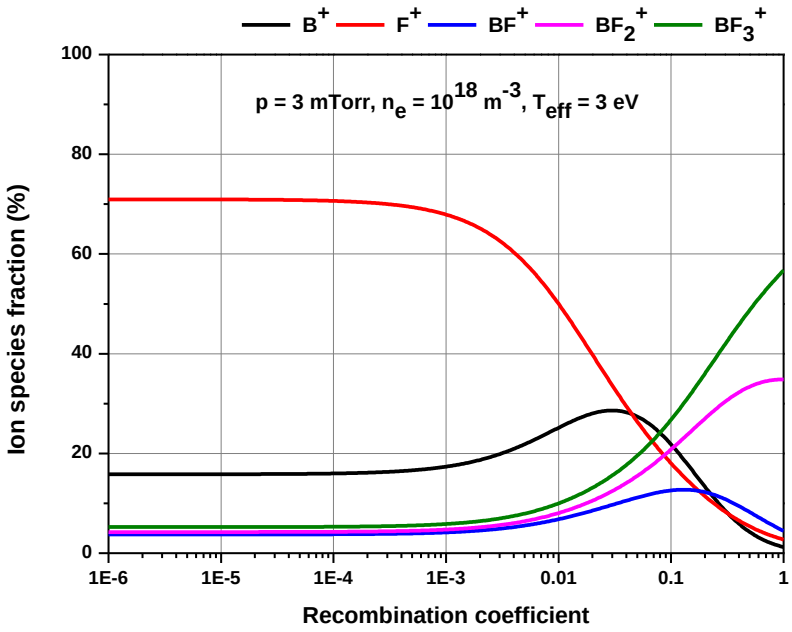


Figure 3.1. The change of ion species fraction by the recombination coefficient when using the experimental data and the Maxwellian electron energy distribution function.

## 3.2. Ion species fractions when changing plasma density

Figure 3.2 describes the variation of ion species fraction when changing the plasma density [12]. The gas pressure p is set as 3 mTorr, the recombination coefficient $\gamma$ 0.01, and the effective electron temperature $T_{eff}$ 3 eV [12]. From Figure 3.2, the ion species fractions of $BF_2^+$ and $BF_3^+$ decrease when increasing the recombination coefficient, but the ion species fraction of $F^+$ increases. The ion species fractions of $B^+$ and $BF^+$ fluctuate. The ion species fraction of $F^+$ is highest in most plasma density values. The ion species fraction of $B^+$ is highest when the plasma density $n_e$ is approximately from $1.26 \times 10^{17}$ $m^{-3}$ to $2 \times 10^{17}$ $m^{-3}$. When the plasma density $n_e$ is from $10^{16}$ $m^{-3}$ to about $1.26 \times 10^{17}$ $m^{-3}$, the ion species fraction of $BF_3^+$ is highest. The plasma density need going up to rise the ion species fraction of $F^+$, but this parameter need going down to rise the ion species fractions of $BF_2^+$ or $BF_3^+$.

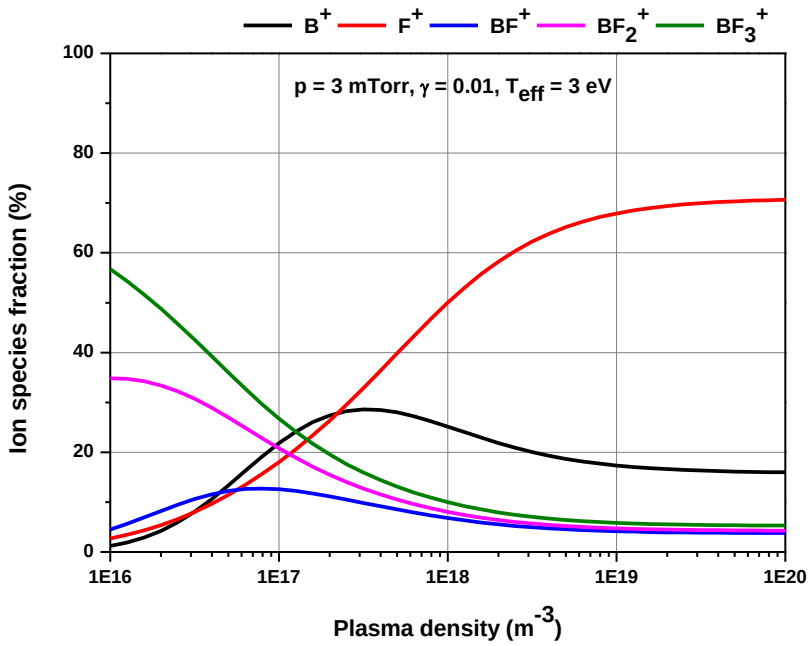


Figure 3.2. The change of ion species fraction by the plasma density when using the experimental data and the Maxwellian electron energy distribution function.

## 3.3. Ion species fractions when changing effective electron temperature

Figure 3.3 describes the variation of ion species fraction when changing the effective electron temperature [12]. The gas pressure p is set as 3 mTorr, the recombination coefficient $\gamma$ 0.01, and the plasma density $n_e$ $10^{18}$ $m^{-3}$ [12]. From Figure 3.3, all of the ion species fractions fluctuate when changing the effective electron temperature. The ion species fraction of $BF_3^+$ is highest when the electrons temperature is from 0.2 to 1.1 eV. The ion species fraction of $B^+$ is highest when the effective electron temperature $T_{eff}$ is from 1.2 to 2.5 eV. The ion species fraction of $F^+$ is highest in all of the remaining effective electron temperature values.

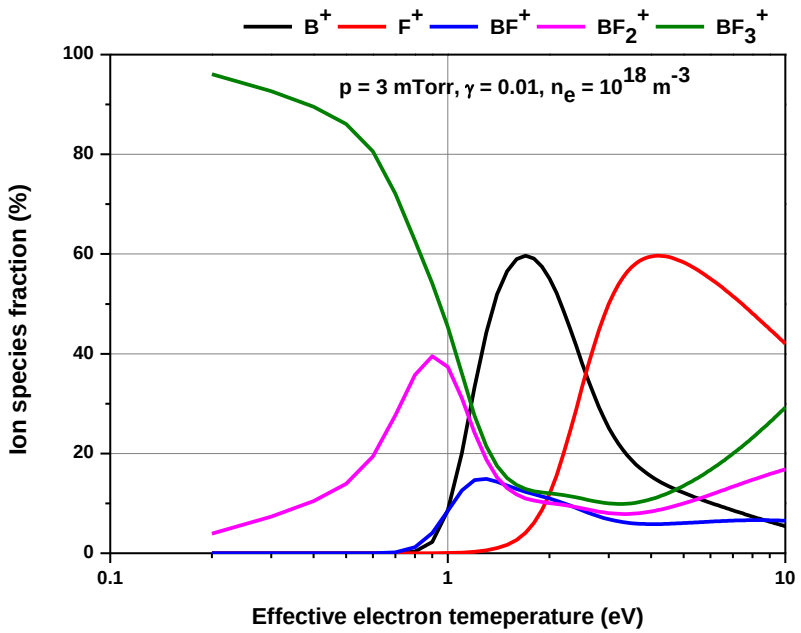


Figure 3.3. The change of ion species fraction by the electron temperature when using the experimental data and the Maxwellian electron energy distribution function.

## 3.4. Ion species fractions when changing high-energy electrons fraction

Figure 3.4 describes the variation of ion species fraction when changing the high-energy electrons fraction [12]. In this case, the high-energy electrons group is included in the model while the Maxwellian electron energy distribution function is still used, so the effective electron temperature is changed because it is calculated from (43) and (44) in section 2.5. The gas pressure p is set as 3 mTorr, the recombination coefficient $\gamma$ is equal to 0 because this parameter is not mentioned, the plasma density $n_e$ $10^{18}$ $m^{-3}$, the low-energy electrons temperature $T_l$ = 3 eV, and the high-energy electrons temperature $T_h$ = 20 eV [12]. From Figure 3.4, when increasing the high-energy electrons fraction, the effective electron temperature increases. The ion species fractions of $B^+$ and $F^+$ go down when rising the high-energy electrons fraction, while the ion species fractions of $BF_2^+$ and $BF_3^+$ go up. The ion species fraction of $BF^+$ fluctuates when changing the high-energy electrons fraction. The ion species fraction of $F^+$ is highest when the high-energy electrons fraction is from 0 to about 55%, while that of $BF_3^+$ is highest in the remaining high-energy electrons fraction values. The ion species fraction of $BF^+$ when the high-energy electrons fraction is from 0 to about 35%, while that of $B^+$ is lowest in the remaining high-energy electrons fraction values. The high-energy electrons fraction need to be reduced to increase the ion species fraction of $B^+$ or $F^+$, but this parameter need to be risen to go up the ion species fractions of $BF_2^+$ or $BF_3^+$.

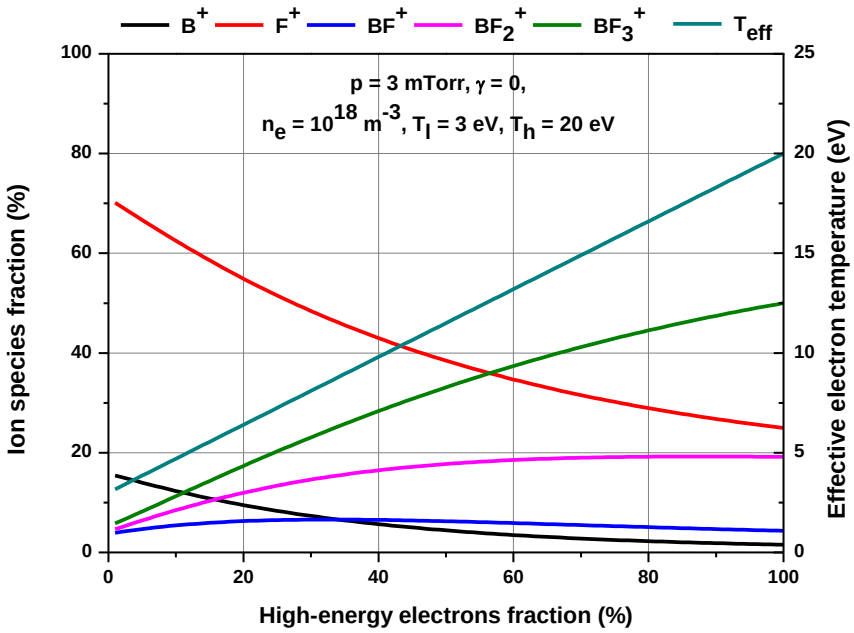


Figure 3.4. The change of ion species fraction by the high-energy electrons fraction when using the experimental data and the Maxwellian electron energy distribution function.

# Chapter 4. Calculation results of the model by using the non-Maxwellian electron energy distribution function when including the high-energy electrons

## 4.1. Ion species fractions when changing the ratio between high-energy electrons density and low-energy electrons density

In this chapter, the dependence of ion species fractions on the electron density and the electron temperature will be considered similar to Chapter 3, but the non-Maxwellian electron energy distribution function will be used. The factors of the Maxwellian electron energy distribution function which are used to describe the non-Maxwellian electron energy distribution function are: $n_{l,0}$ = $10^{18}$ $m^{-3}$, $T_l$ = 3 eV, $n_{h,0}$ = $10^{17}$ $m^{-3}$, and $T_h$ = 20 eV.

Figure 4.1 describes the variation of ion species fraction when changing the ratio between the high-energy electrons density $n_{h,0}$ and the low-energy electrons density $n_{l,0}$ by using the non-Maxwellian electron energy distribution function [12]. The gas pressure p is set as 3 mTorr, and the recombination coefficient $\gamma$ is equal to 0 because this parameter is not mentioned [12]. The factors of the Maxwellian electron energy distribution function which are used to describe the non-Maxwellian electron energy distribution function are mentioned above. From Figure 4.1, the ion species fractions of $B^+$ and $F^+$ when increasing the ratio between high-energy electrons density and low-energy electrons density, while the species fractions of $BF_2^+$ and $BF_3^+$ increase. The ion species fraction of $BF^+$ fluctuates when changing the

ratio between high and low-energy electrons densities. The ion species fraction of $BF_3^+$ is highest in most of the ratio between high and low-energy electrons densities values. When the ratio between high and low-energy electrons densities is from 0 to approximately 13%, the ion species fraction of $F^+$ is highest. The ratio between high and low-energy electrons densities need to be fallen to go up the ion species fraction of $B^+$ or $F^+$, but this ratio need to be risen to go up the ion species fractions of $BF_2^+$ or $BF_3^+$.

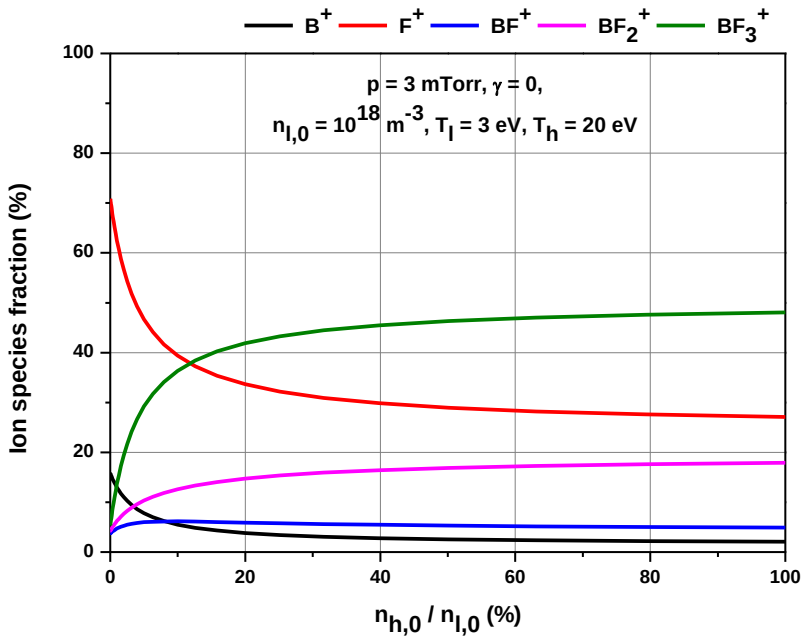


Figure 4.1. The change of ion species fraction by the ratio between the high-energy electrons density and low-energy electrons density when using the non-Maxwellian electron energy distribution function which is given by the sum of the Maxwellian electron energy distribution function.

## 4.2. Ion species fractions when changing low and high-energy electrons temperatures

Figure 4.2 describes the variation of ion species fraction when changing the low-energy electrons temperature $T_l$ by using the non-Maxwellian electron energy distribution function [12]. The gas pressure p is set as 3 mTorr, and the recombination coefficient $\gamma$ is equal to 0 because this parameter is not mentioned [12]. The factors of the Maxwellian electron energy distribution function which are used to describe the non-Maxwellian electron energy distribution function are mentioned above in section 4.1. From Figure 4.2, all of the ion species fractions fluctuate when changing the low-energy electrons temperature. The ion species fraction of $BF_3^+$ is highest in most of the low-energy electrons temperature values. When the low-energy electrons temperature is from 3 to 11 eV, the ion species fraction of $F^+$ is highest. In addition, the dependence of ion species fractions on the low-energy electrons temperature has been reduced when including high-energy electrons group.

Figure 4.3 describes the variation of ion species fraction when changing the high-energy electrons temperature $T_h$ by using the non-Maxwellian electron energy distribution function [12]. The gas pressure p is set as 3 mTorr, and the recombination coefficient $\gamma$ is equal to 0 because this parameter is not mentioned [12]. The factors of the Maxwellian electron energy distribution function which are used to describe the non-Maxwellian electron energy distribution function are mentioned above. From Figure 4.3, all of the ion species fractions fluctuate when changing the high-energy electrons temperature. The ion species fraction of $F^+$ is highest when the high-energy electrons temperature is from 3 to about 20 eV. The ion species fraction of $BF_3^+$ is highest in all of the remaining high-energy electrons temperature values.

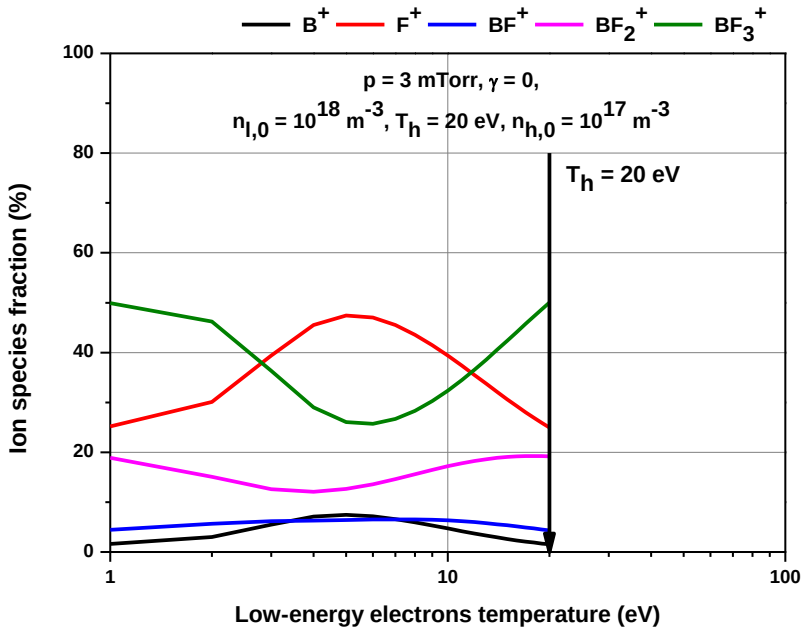


Figure 4.2. The change of ion species fraction by the low-energy electrons temperature when using the non-Maxwellian electron energy distribution function which is given by the sum of the Maxwellian electron energy distribution function.

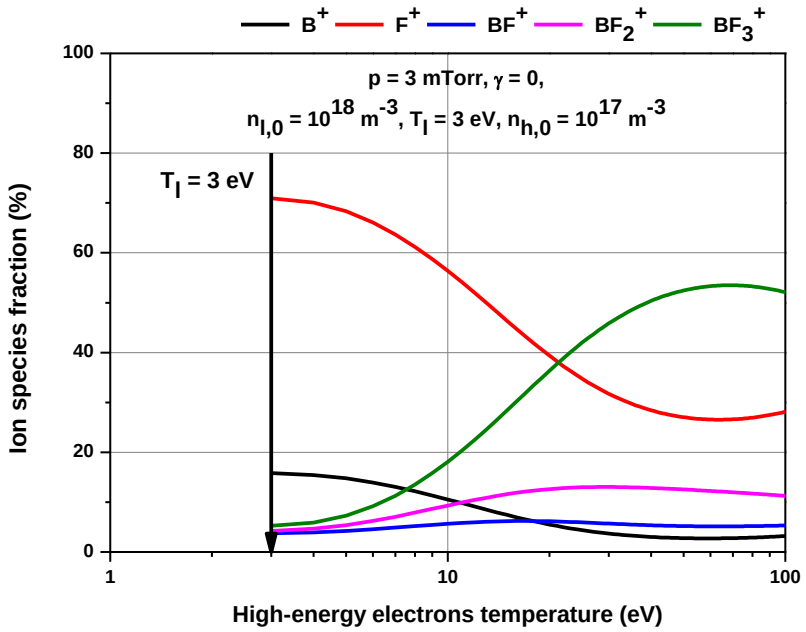


Figure 4.3. The change of ion species fraction by the high-energy electrons temperature when using the non-Maxwellian electron energy distribution function which is given by the sum of the Maxwellian electron energy distribution function.

# Chapter 5. Conclusions and Future Works

In this thesis, the global model is built to identify the ion species fractions. From the calculation results of the ion species fractions based on the global model, there are some limitations in both of the previous work (or Patel's work) with the present work and some differences of building the model in the thesis compared to Patel's model. Firstly, in Patel's work [2, 3], the Maxwellian electron energy distribution function and the multi-cusp magnetic field effect of the ULE2 ion source are included, while in our work, the experimental EEPF data are measured in the presence of the axial magnetic field of the PIG source. Secondly, for the chemical processes of the model, the momentum transfer, the charge transfer, and the excitation processes, including the vibrational excitation reactions in Patel's model [2] are also ignored. Thirdly, the $BF_3$ secondary reactions in Patel's model [2] are also ignored to simplify the calculation. Most of the present rate constants data are obtained by using the different cross-section data compared to Patel's calculation results [2, 3], such as the ionization of $BF_3$, $BF_2$, BF, B (by using the NIST data [5, 6] because of this highly accurate level) and F (by using the Approximate Analytic Formula (AAF) [7, 20]), but they are not fit to the Arrhenius form [2] when performing the calculations. Furthermore, in the present rate constants data, the value of electron temperature is from 1 to 100 eV, while in Patel's work, this value is from 1 to 8 eV. The reason for this difference is using the cross-sections data allows us to calculate the rate constants with the electron temperature larger than 8 eV. That is the limitation of Patel's work. The ion species fractions are calculated by using the Maxwellian electron energy distribution function and the non-Maxwellian electron energy distribution function which is given by the sum of the Maxwellian energy distribution function. The important contribution in

this thesis is using the experimental electron energy probability function (EEPF) or the non-Maxwellian electron energy distribution function to calculate the rate constant. In our code, the recombination coefficient, the electron density, and the electron temperature have important roles for calculating the ion species fraction. When using the Maxwellian electron energy distribution function, the recombination coefficient need falling or the plasma density need rising or the high-energy electrons fraction need falling to increase the ion species fraction of $F^+$. However, the recombination coefficient need going up or the plasma density need going down or the high-energy electrons fraction need going up to rise the ion species fractions of $BF_2^+$ or $BF_3^+$. The high-energy electrons fraction need going down to rise the ion species fraction of $B^+$. When using the non-Maxwellian electron energy distribution function, the ratio between high and low-energy electrons densities need reducing to increase the ion species fraction of $F^+$. In the case of rising the ion species fraction of $B^+$, the high-energy electrons density should be reduced. The high-energy electrons density need going up to go up the ion species fractions of $BF_2^+$ or $BF_3^+$. Furthermore, the dependence of ion species fractions on the low-energy electrons temperature has been reduced when including high-energy electrons group.

In the future, the power balance equation, the transport phenomena, and the axial magnetic field effect of the ion source (throughout the edge-to-center density ratio) will be included in the model to make more accurate results and compare the obtained plasma densities and electron temperatures to the experimental data to find out the differences between the theory numerical model and the experimental results, which leads to understanding the importance of $BF_3$ global model in the semiconductor industry.

# Bibliography


[1] B. Wolf (ed), “Handbook of Ion Sources”, Boca Raton, FL: CRC Press (1995).

[2] K. Patel, “Volume averaged modeling of high density discharges” (thesis, U. C. Berkeley, 1998).

[3] M. A. Graf, V. Benveniste, M. A. Lieberman, K. Patel, “A Global Model for $BF_3$ Plasma in a RF-Driven Multicusp Ion Source”, IEEE Xplore, International Conference on Ion Implantation Technology Proceedings, Kyoto, Japan (1998).

[4] M. A. Lieberman, A. J. Lichtenberg, “Principles of Plasma Discharges and Materials Processing” (Wiley Interscience, New York, 2005).

[5] URL for NIST website: https://www.nist.gov/pml/electron-impact-cross-sections-ionization-and-excitation-database (2004).

[6] Y.-K. Kim, J. P. Santos, F. Parente, “Extension of the binary-encounter-dipole model to relativistic incident electrons”, Phys. Rev. A **62**, 052710 (2000).

[7] M. A. Lennon, K. L. Bell, H. B. Gilbody, J. G. Hughes, A. E. Kingston, M. J. Murray, F. J. Smith, “Recommended Data on the Electron Impact Ionization of Atoms and Ions: Fluorine to Nickel”, J. Phys. Chem. Ref. Data 17, 1285 (1988).

[8] Y. S. Hwang, K. -J. Chung, J. Y. Kim, J. Y. Choi, G. W. Go, “PIG Ion Source Study” (2020).

[9] J. Y. Kim, J. Y. Jang, J. Y. Choi, J. -I. Wang, W. I. Jeong, M. A. I. Elgarhy, G. W. Go, K. -J. Chung, Y. S. Hwang, "Magnetic Confinement and Instability in Partially Magnetized Plasma", Plasma Sources Sci. Technol. 30, 025011 (2021).

[10] J. Y. Kim, D. -H. Kim, J. H. Kim, S. -B. Jeon, S. -W. Cho, C. -W. Chung, "Power dependence of electron density at various pressures in inductively coupled plasmas", Physics of Plasmas 21, 113505 (2014).

[11] O. Fukumasa, R. Itatani, S. Saeki, "Numerical simulation of hydrogen ion species in the steady-state plasma of a low-pressure ion source", J. Phys. D: Appl. Phys. 18, 2433-2449 (1985).

[12] K. Choe, "Development of Hydrogen Cold Cathode Penning Ion Source in Pulsed Operation with High Monoatomic Fraction" (thesis, Seoul National University, 2018).

[13] R. Zorat, J. Goss, D. Boilson, D. Vender, "Global model of a radiofrequency $H_2$ plasma in DENISE", Plasma Sources Sci. Technol. 9, 161-168 (2000).

[14] H. -C. Lee, C. -W. Chung, "Effect of Electron Energy Distribution on the Hysteresis of Plasma Discharge: Theory, Experiment, and Modeling", Scientific Reports (2015).

[15] A. R. Martin, T. S. Green, Culham Lab. Rep. CLM-R159 (1976).

[16] Van Duy Cung, K. -J. Chung, and Y. S. Hwang, "Development of a global model for $BF_3$ discharge", Transactions of the Korean Nuclear Society Spring Meeting, Jeju, Korea (2020).

[17] The data summary final of the PIG source, including the experimental EEPF data, the effective electron temperature, and the plasma density is obtained from J. Y. Kim and J. Y. Choi.

[18] Y. Zhang, C. Charles, and R. Boswell, “Cross-field transport of electrons at the magnetic throat in an annular plasma reactor”, J. Phys. D: Appl. Phys. 50, 015205 (2017).

[19] H. Zhang (ed), “Ion Sources”, New York: Science Press, Springer (1999).

[20] K. L. Bell, H. B. Gilbody, J. G. Hughes, A. E. Kingston, F. J. Smith, “Recommended Data on the Electron Impact Ionization of Light Atoms and Ions”, J. Phys. Chem. Ref. Data 12, 891 (1983).

# 국문 초록

저압 영역대 $BF_3$ 플라즈마의 이온 종 비율을 도출하기 위한 글로벌 0차원 계산 모델을 개발하였다. 본 단순 모델은 입자 평형, 전하량 보존 및 입자 총량 보존을 고려하여 작성되었으며, 그 중 이온종 비율을 계산하기 위해 제일 중요하게 고려한 요소는 전자 밀도, 유효 전자 온도, 그리고 이온 재결합 계수이다. 특히, 저압 방전 영역대의 비 맥스웰 분포를 가진 전자의 거동을 반영하기 위하여, 전자는 크게 두 가지 종으로 구분되어 각각의 비율을 조정하여 이온종이 그 두 종류 전자의 비율에 대해 어떻게 변화하는지 관측하였다.

본 주제의 주 목적은 재결합 계수가 주어지지 않았을 때, 저 에너지 전자 그룹을 고정시키고 고 에너지 전자 그룹을 포함하여 이온종의 변화를 관측하는 것이다. 그리고 본 주제에 가장 기여도가 큰 부분은 비 맥스웰 분포를 가지는 전자 모델을 이용하여 계수를 구한 것이다. 저 에너지 전자만을 이용한 계산은 전자 온도가 이온 빔 비율에 높은 감도를 가진다는 것을 알 수 있었으며, 이는 고 에너지 전자를 계산에 추가하여 낮출 수 있었다. 또한, 재결합 계수가 해당 모델에 큰 영향을 미친다는 것도 확인할 수 있었다. 재결합 계수가 0에 가까워야 원하는 이온 종의 생산이 가능하다는 것을 알 수 있었는데, 이는 중성 입자들의 상태가 챔버 벽의 경계면과 상호작용할 때 거의 변화하지 않는다는 것을 의미한다.

**주요어:** 이온 종 분율, $BF_3$ 방전, 입자 평형 방정식, 전하 보존.

**학 번:** 2018-27587